Available online at www.sciencedirect.com

ScienceDirect

journal homepage: www.elsevier.com/locate/he

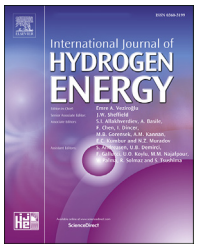

Mechanism of methanol decomposition on the Cu-Embedded graphene: A DFT study

Aykan Akça [a,****], *Onur Karaman* [b], *Hassan Karimi-Maleh* [c,*], *Fatemeh Karimi* [c,**], *Ceren Karaman* [d,***], *Necip Atar* [e], *Mehmet Lütfi Yola* [f], *Nevin Erk* [g]

[a] *Aksaray University, Faculty of Science and Letters, Department of Physics, Aksaray, Turkey*
[b] *Akdeniz University, Vocational School of Health Services, Department of Medical Services and Techniques, Antalya, Turkey*
[c] *Department of Chemical Engineering and Energy, Laboratory of Nanotechnology, Quchan University of Technology, Quchan, Islamic Republic of Iran*
[d] *Akdeniz University, Vocational School of Technical Sciences, Department of Electricity and Energy, Antalya, Turkey*
[e] *Pamukkale University, Faculty of Engineering, Department of Chemical Engineering, Denizli, Turkey*
[f] *Hasan Kalyoncu University, Faculty of Health Sciences, Department of Nutrition and Dietetics, Gaziantep, Turkey*
[g] *Ankara University, Faculty of Pharmacy, Department of Analytical Chemistry, 06560, Ankara, Turkey*

HIGHLIGHTS

- Decomposition of methanol on the CuG surface has offered low activation barriers.
- Cu embedding on the graphene boost the catalytic activity.
- $CH_3OH. \rightarrow CH_3O \rightarrow CH_2O \rightarrow CHO \rightarrow CO$ path is the most likely pathway
- CuG would significantly reduce the catalyst cost.
- CuG can utilized as an alternative catalyst to reduce the CO poisoning problem.

ARTICLE INFO

Article history:
Received 2 August 2021
Received in revised form
26 August 2021
Accepted 6 September 2021
Available online 20 September 2021

Keywords:
Density functional theory
Cu-embedded graphene
Methanol decomposition
Reaction mechanism

ABSTRACT

The methanol decomposition reaction has gained substantial attention due to the wide range of applications that its intermediates offer. In this work, methanol (CH_3OH) decomposition on Copper-embedded graphene (CuG) surface has been investigated via density functional theory with Grimme-D2 dispersion correction. The charge density of the CuG surface has been analyzed and the redistribution of the electron density of the surface has been represented via the electron density difference (EDD) map. Moreover, the decomposition reaction mechanism of CH_3OH on the CuG surface through the cleavage of C–H, O–H and C–O bonds has been investigated in detail. In the initial state, the C–O and O–H bonds of CH3OH have similar activation barriers, thereby the adsorption and degradation mechanism of the intermediate states arising through O–H bond cleavage on the CuG surface has been investigated. In addition, the charge density calculations of the transition state geometries have been conducted and examined with EDD maps. The

* *Corresponding author.*
** *Corresponding author.*
*** *Corresponding author.*
**** *Corresponding author.*
E-mail addresses: aykanakca@aksaray.edu.tr (A. Akça), h.karimi.maleh@qiet.ac.ir (H. Karimi-Maleh), fkm024@qiet.ac.ir (F. Karimi), cerenkaraman@akdeniz.edu.tr (C. Karaman).
https://doi.org/10.1016/j.ijhydene.2021.09.028

results have revealed that the previously adsorbed oxygen molecule exhibited high catalytic activity towards O–H decomposition compared to the bare surface. The CuG surface has offered higher activity on the C–H bonds compared to the C–O bonds of the intermediate states generated by CH_3OH decomposition. The results revealed that the proposed CuG structure can be utilized as an alternative electrode catalyst that can prevent the CO poisoning issue in direct methanol fuel cells.

Introduction

The development of alternative renewable technologies such as fuel cells for ensuring the long-term energy sustainability has garnered considerable attention as a way to cope with the environmental concerns caused by the usage of fossil fuels [1–3]. Hydrogen is now widely regarded as a clean and feasible energy source for power production in both portable and large-scale applications [4–6]. However, due to the obvious constraints of hydrogen storage systems, the fabrication of onboard hydrogen using liquid fuels such as methanol is gaining popularity as a means of developing fuel cell-powered devices [7]. Methanol decomposition is one of the crucial processes in the state-of-art direct methanol fuel cell (DMFC) technology, as well as research and development works in chemical industry [8,9]. Moreover, it has been receiving substantial attention from the scientific community due to the potential broad applications of its end products [10]. Methanol is of great potential to be utilized as a reactant for various chemical processes as well as an energy carrier for hydrogen storage and transportation [11,12]. Besides, it has been regarded as one of the most encouraging alternative energy sources thanks to its abundance, cost-natural feature, and enhanced safety [13]. Although the usability of methanol as an alternative energy source has been studied in detail since the first oil crisis in 1973, much more research is needed before it can be used in the current DMFC technology and conventional internal combustion engines [8]. Previous works in the literature have reported that noble metals such as Pt, Pd, Ru, Ir, etc. are the high-performance catalysts that can be utilized to facilitate the catalytic decomposition of methanol to hydrogen and syngas [14–22]. In particular, for DMFC, even though the noble metal-based nanocatalysts have been shown to have high catalytic activity for the methanol decomposition reaction, they are suffering from poor resistance to both sintering and CO poisoning [23–25]. Therefore, the engineering of high-performance catalysts to be utilized for methanol decomposition reaction as an alternative to noble metal catalysts is of great importance.

In the catalytic decomposition of methanol, the methoxy radical (CH_3O) is the first intermediate species in the hypothesized mechanism (Eq. (1)) which has been studied extensively and supported by experimental data [18,26–30]. Therefore, dehydrogenation of the alcoholic group of methanol is expected to be the initial step in the methanol decomposition process.

$$CH_3OH_{gas} \rightarrow CH_3OH_{ads} \rightarrow CH_3O_{ads} \rightarrow CH_2O_{ads} \rightarrow CHO_{ads} \rightarrow CO_{ads} \quad (1)$$

Indeed, recent experimental evidence has verified that the rate of this process is sufficiently high at ambient temperature and the low-pressure range since complete dehydrogenation of methanol to CO on noble metal catalyst surfaces is observed at *ca.*200 K [18]. As a result, comprehending the energy of this process paves the way for understanding the fundamental step of the methanol decomposition mechanism. Therefore, it should be emphasized that a detailed study of the catalyst surface chemistry along with the methanol decomposition mechanism is of great importance in the design of superior performance catalysts. From past to present, energetically optimal reaction pathways have been investigated to elucidate the reaction mechanism of the methanol decomposition reaction [31–34]. Nevertheless, due to its dependence on the catalyst surface characteristics, the enlightenment of the reaction mechanism is still elusive, thereby new approaches such as computational methods should be evolved and refined.

Among the various type of carbon-based-catalysts, graphene, a peculiar class of two-dimensional (2D) carbonaceous materials with superior physicochemical properties, has been considered to be a preferred alternative catalysts-support since it offers excellent catalytic activity in fuel cells [25,35–43]. Moreover, graphene and its derivatives own outstanding properties including high surface areas with a large amount of electrocatalytic active sites, controllable pore structure, temperature resistivity, and specific metal-support interaction [44–47] which have been extensively utilized as supporting scaffold for heterogeneous catalysts in various catalytic processes such as oxygen reduction reaction [48–51], N_2O reduction [52–54], hydrogen evolution reaction [55–57], methanol oxidation [58] CO oxidation [59,60], NH_3 decomposition [61–63], etc. The charged zone created in the center of the graphene surface by inserting transition metal atoms or heteroatoms onto the structure can be employed as the electrocatalytically active sites for catalytic processes [64–66]. Furthermore, the highly stable structures of metal-embedded graphene networks, as well as the strengthen the interactions between the metal and the nearest carbon atoms, make them

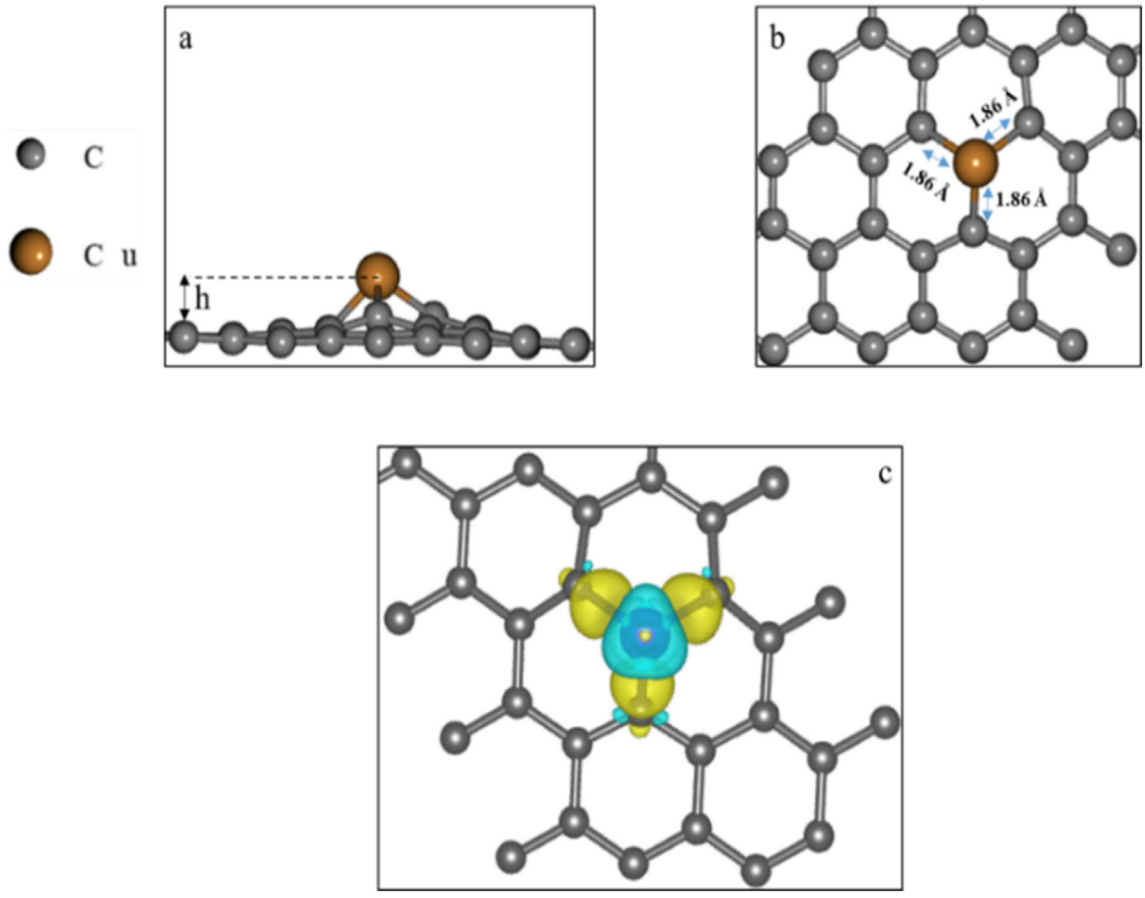

Fig. 1 – (a) Side, and (b) Top view of the CuG surface; (c) EDD map (±0.006 au) of the CuG surface.

suitable candidate for catalytic processes [67]. The previously reported similar researches have emphasized that the coordinated metal clusters on graphene sheets have lower activation energies than the pristine clusters [68]. Among these structures, the Cu-embedded graphene networks have already been employed in numerous (electro)catalytic processes with superior catalytic activity and relatively cheaper cost [69–73].

Methanol decomposition on Cu(111), (110), and (100) surfaces has been studied before using theoretical calculations [74,75]. All of the findings have been beneficial in the design and optimization of Cu-based catalysts using computational methods. Hence, it is possible to speculate that Cu-embedded graphene networks might be a contender alternative catalyst for the catalytic decomposition of methanol. However, to the best of our knowledge, no mechanistic investigation of catalytic decomposition of methanol on Cu-embedded graphene surface has been demonstrated yet.

Bearing all aforementioned points in mind, herein, the potential utilization of Cu-embedded graphene surface as an alternative catalyst in catalytic decomposition of methanol has been investigated by density functional theory with Grimme-D2 dispersion correction, as well as the possible reaction mechanism has been comprehensively enlightened. A detailed explanation of the adsorption energies, reaction mechanisms of the most likely pathways, and surface catalytic activity. It can be speculated that the findings of this work will fill the gap in this field and shed light on the engineering of high-performance catalysts that can be a substitute for noble metal-based catalysts to be utilized in the catalytic methanol decomposition reaction.

Computational details

In this work, the Quantum Espresso software package was used to compute all data by using density functional theory [76,77]. PAW potential was preferred with non-linear core correction and the scalar relativistic correction, to eliminate core electrons and an unusually large number of plane waves that serve oscillations close to atomic nuclei [78]. GGA-PBE

Table 1 – Some physical parameters were acquired for the Cu-embedded graphene layer.

Parameters	This Work (QE)	Ref. [84]
Elevation-h (A)	1.72	1.78
Bond Lengths (A) (Ni–C)	1.87	1.88
Magnetic Mom. (μ_B)	0.93	1
Binding Energy (E_B) (eV)	−3.92	−3.69
Cu, C1, C2, C3 charges, |e|	+0.65, −0.25, −0.24, −0.20	Not reported

functional was used to define the exchange correlation term [79]. The kinetic energy cutoff value of 700 Ry was used for charge density interactions and potential and the kinetic energy cutoff 70 Ry values were used for wave functions. Brillouin zone samples (samplings) were used 4 × 4 × 1 Monkhorst-Pack k-points. Grimme-D2 correction applied to observe the weak interactions between surface and reactants [80]. In all calculations, mixing beta and degauss values were determined as 0.7 and 0.07 Ry, respectively. The lattice parameters of the selected graphene surface were determined as a = 9.8 Å and c = 20 Å. A three-dimensional (3D) box with a lateral length of 15 A^3 was used for the optimization of the gas phase structures. For all of the calculations, the force and energy convergence criteria were determined as 1×10^{-5} Ry/atom and 1×10^{-6} Ry/atom, respectively. The spin polarized effect was considered in all calculations. The partial charge densities were calculated by Bader charge analysis [81]. The VESTA program was run to display the EDD maps. The adsorption energies of the reactants on the surface was calculated by Eq. (2).

$$E_{ads} = E_{adsorbates/surface} - (E_{surface} + E_{adsorbates}) \quad (2)$$

where $E_{adsorbates/surface}$ represents the total energy of adsorbate structures adsorbed on the surface, $E_{surface}$ stands for the total energy of the bare/bare surface, and $E_{adsorbates}$ is the total energy of adsorbate structures in the gas phase.

Climbing image-nudged elastic band (CI-NEB) [82] method was implemented for the transition state calculations and obtaining the transition state geometries.

The activation (E_A) and reaction (E_R) energies of the intermediate states that compose the reaction mechanism were calculated using Eq. (3) and Eq. (4), respectively.

$$E_A = E_{TS} - E_{IS} \quad (3)$$

$$E_R = E_{IS} - E_{FS} \quad (4)$$

here E_{IS} and E_{FS} represent the initial and final state energies of the intermediate states, respectively, whereas E_{TS} is the transition state energy.

Results and discussion

The modelling of Cu-embedded graphene surface from pristine graphene

It is critical to achieve the most stable geometric structure of the catalyst surface in order to determine the catalytic activity and selectivity of the catalysts on a chemical process. Furthermore, because metal-doped graphene supercells constructed using periodic boundary conditions have high surface areas, the detrimental effect of lateral interactions on total energy and energy barriers estimates can be avoided. Herein, firstly, a graphene sheet consisting of 32 carbon atoms was obtained from the bulk cell of graphite, with the nearest carbon atoms distance (C–C) 1.42 Å [83]. Subsequently, by removing the carbon atom in the center of the graphene and introducing copper (Cu) atom instead, Cu-embedded graphene (CuG) surface (Cu1/C31) was obtained. The most stable geometric structure of the CuG surface were represented in Fig. 1a and b.

Some important parameters obtained for the CuG surface were tabulated in Table 1 and compared with the results of other similar studies in the literature. Fig. 1c also depicted the EDD map derived from the Bader charge analysis results. The yellow and blue regions on the EDD map represented the gained and lost electron regions, respectively. Accordingly, the regions highlighted in yellow implied the electron transfer from the Cu atom and to the nearest carbon atoms, and thereby, strong covalent bonding occurs between the Cu–C atoms. On the other hand, the blue region represented the region of positive charge accumulated around the Cu atom after electron transfer. This charge transfer led the Cu atom to have a value of +0.65|e|.

Adsorption of intermediate state molecules onto the CuG surface

The most stable adsorption geometries obtained for all possible intermediate states that might occur during the decomposition of methanol on the CuG surface were

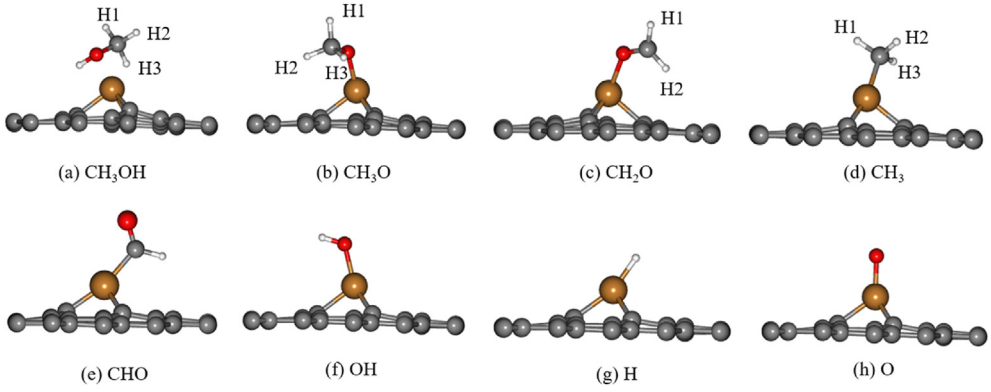

Fig. 2 – The adsorption geometries of (a)CH_3OH,(b) CH_3O, (c) CH_2O, (d) CH_3, (e) CHO, (f)OH, (g)H, and (h)= intermediate states on Cu-G surface.

Table 2 – Some important parameters obtained for intermediate states adsorbed on to the CuG surface.

Species	E_{ads}	Bond lengths	
	Cu-G	Gas phase (Å)	Adsorbed on Cu-G (Å)
CH_3OH	−0.86	C–H1 = 1.10	C–H1 = 1.1
		C–H2 = 1.09	C–H2 = 1.09
		C–H3 = 1.10	C–H3 = 1.1
		O–H = 0.97	O–H = 0.98
		C–O = 1.43	C–O = 1.46
CH_3O	−2.56	C–H1 = 1.10	C–H1 = 1.10
		C–H2 = 1.10	C–H2 = 1.11
		C–H3 = 1.10	C–H3 = 1.11
		C–O = 1.35	C–O = 1.40
CH_2O	−1.04	C–H1 = 1.12	C–H1 = 1.10
		C–H2 = 1.2	C–H2 = 1.10
		C–O = 1.21	C–O = 1.26
CH_3	−2.07	C–H1 = 1.09	C–H1 = 1.10
		C–H2 = 1.09	C–H2 = 1.10
		C–H3 = 1.09	C–H3 = 1.10
CHO	−1.92	C–H = 1.13	C–H = 1.14
		C–O = 1.21	C–O = 1.19
OH	−3.14	O–H = 0.98	O–H = 0.97
O	−3.61	–	H–Cu = 1.68
H	−2.17	–	O–Cu = 1.54

displayed in Fig. 2. Moreover, some important parameters for all possible geometries adsorbed on the CuG surface were listed in Table 2.

As shown in Fig. 2a, CH_3OH was adsorbed horizontally to the surface, and the it preferred to be bounded to the CuG surface via the O atom. The adsorption energy of the CH_3OH molecule to the surface was calculated to be −0.86 eV.

For the CH_3O, it preferred to be bound to the CuG surface from the O side with an adsorption energy of −2.56 eV (Fig. 2b). Furthermore, according to the parameters tabulated in Table 2, C–H1, C–H2, C–H3 and C–O bonds were found to be more activated compared to the gas phase.

Similarly, the formaldehyde (CH_2O) was also bound to the CuG surface by the O side with an adsorption energy of −1.04 eV, and the most stable adsorption geometry of CH_2O was shown in Fig. 2c. According to the obtained values in the gas phase, while the C–H1 and C–H2 bonds of CH_2O adsorbed on the surface were shortened, the bond between C–O was elongated.

On the other hand, the most stable adsorption geometry of the methyl group (CH_3) was the one configuration in which it was bonded to the surface by the carbon atom. The adsorption geometry of the CH_3 adsorbed to the surface was depicted in Fig. 2d. It was found that the CH_3 was bound to the CuG surface with an adsorption energy of −2.07 eV. In addition, according to Table 2, it was determined that the C–H1, C–H2 and 1.10 C–H3 bonds elongated slightly compared to the gas phase.

The CHO molecule preferred to be adsorbed on the CuG surface by the carbon atom (Fig. 2e) and the adsorption energy of the CHO molecule was found to be −1.92 eV. On the other hand, as can be seen from Fig. 2f, OH radical preferred to be bound to the CuG surface from the O side with an adsorption energy of −3.14 eV. Moreover, O and H atoms were bound to the CuG surface with adsorption energies of −3.61 eV and −2.13 eV, respectively. The adsorption geometries of the both atomic structures on the CuG surface were shown in Fig. 2g and h. Additionally, the bond lengths between O–Cu and H–Cu were found to be 1.68 Å and 1.54 Å, respectively.

The co-adsorption of intermediate species on Cu embedded graphene

In this section, the co-adsorption nature of possible intermediate states that may occur during the CH_3OH decomposition reaction was investigated. All co-adsorption geometries were obtained considering the individual adsorption geometries that compose them (Fig. 3). Moreover, the calculated co-adsorption energy values for all possible intermediate states were listed in Table 3. The co-adsorption energies (E_{co-ads}) were calculated by means of the Eq. (4),

$$E_{co-ads} = E_{gas}\,(A) + E_{gas}\,(B) + E_{(slab)} - E((A/B) - E_{slab}) \quad (4)$$

where, E_{gas} (A) + E_{gas} (B) represents the total energies of A and B species obtained in the gas phase. E_{slab} is the total energy of CuG surface whereas E ((A/B) − E_{slab}) stands for the total energy of the co-adsorption species on the CuG surface.

For CH_3O + OH, it was observed that the CH_3O and OH radical preferred to be bound together around the central Cu atom of the surface (Fig. 3a). According to the most stable co-adsorption geometry, the distance between CH_3O–OH was calculated as to be 2.67 Å, while the surface binding energy of CH_3O + OH was −4.55 eV. Similarly, as can be seen from Fig. 3b for CH_3OH + O, CH_3OH and O preferentially bond around the Cu atom with co adsorption energy of −3.93 eV. According to this geometry, the stable distance between CH_3OH–O was found to be 2.81 Å. On the other hand, in the case of CH_3+OH, CH_3 and OH radical CuG favored being bound to the surface by −4.44 eV co-adsorption (Fig. 3c). In this geometry, CH_3 was bound to the surface by carbon, while the OH radical was attached to the surface by oxygen. The most stable equilibrium distance of CH_3–OH was found to be 2.76 Å. Moreover, in the case of CH_3O + H, the stable equilibrium distance between CH_3O and H species was obtained as to be 2.45 Å (Fig. 3d). According to this co-adsorption geometry, CH_3O and H preferred to bind around Cu atom with a co-adsorption energy of −3.98 eV.

In the co-adsorption geometry of the CH_3+O species, the CH_3 molecule favored being bound to the Cu atom, whereas the O atom preferred to bind to the carbon atom closest to the Cu atom (Fig. 3f). The stable equilibrium distance between CH_3–O was obtained as to be 3.14 Å. It was also bound to the surface with a co-adsorption energy of −6.57 eV.

For CH_2O + H, the stable equilibrium distance between CH_2O and H was determined to be 2.66 Å. The co-adsorption geometry (Fig. 3e) revealed that CH_2O was attached to the Cu atom on the surface, while the H atom preferred to bind to the carbon atom closest to Cu atom. In addition, CH_2O and H were bound to the surface with a co-adsorption energy of −3.31 eV.

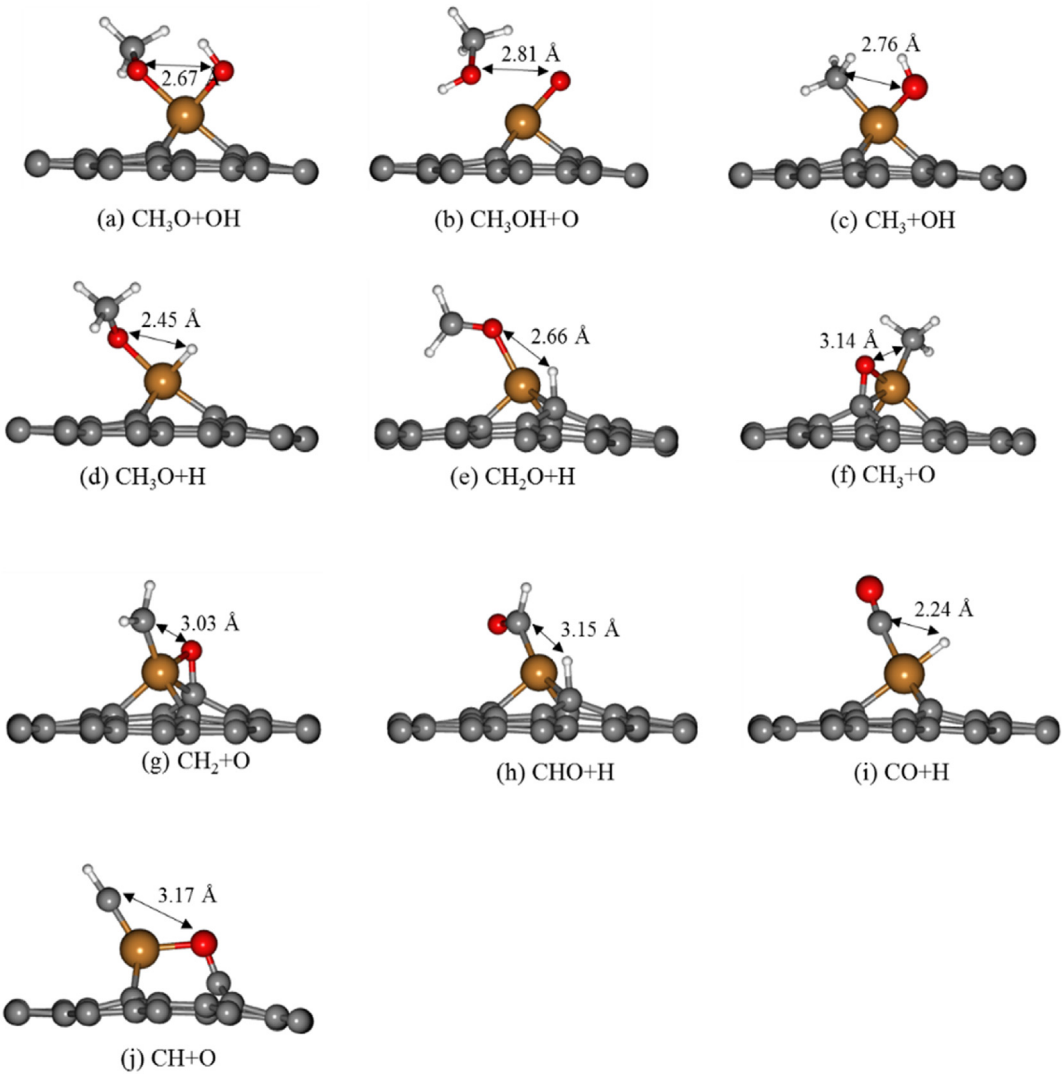

Fig. 3 – The co-adsorption geometries of (a) CH_3O+OH, (b) CH_3OH+O, (c) CH_3+OH, (d) CH_3O+H, (e) CH_2O+H, (f) CH_3+O, (g) CH_2+O, (h) CHO+H, (i) CO+H, and (j) CH+O intermediate states on Cu-graphene surface.

Table 3 – Co-adsorption energies for related intermediates on Cu-G surface.

Species	E_{ads}/eV
$CH_3OH + O$	−3.93
$CH_3O + OH$	−4.55
CH3+OH	−4.44
$CH_3O + H$	−3.98
CH_3+O	−6.57
$CH_2O + H$	−3.31
CHO + H	−4.20
CH_2+O	−7.29
CH + O	−7.24
CO + H	−3.09

For CH_2+O species, the stable equilibrium distance of both molecules on the CuG surface was found to be 3.03 Å. In this geometry, while the CH_2 molecule was adsorbed on the surface by the carbon, the O atom preferred to co-adsorb to both Cu and the nearest carbon atom (Fig. 3g). The co-adsorption energy of the CH_2+O species to the surface was calculated as −7.29 eV.

As can be seen from Fig. 3h, in the case for CHO + H species, the CHO molecule was adsorbed by the carbon on the surface, while the H atom preferred to be adsorbed to the carbon atom closest to the Cu atom. The stable equilibrium distance between CHO and H in the co-adsorption geometry was found to be 3.15 Å, and the co-adsorption energy was −4.20 eV.

As shown in Fig. 3i, CO and H species tended to be adsorbed together around the Cu atom on the CuG surface. While the stable equilibrium distance between CO–H was found to be 2.24 Å, the co-adsorption energy of CO + H to the surface was determined as −3.09 eV.

For CH + O, CH molecule preferred to be adsorbed to the CuG surface by the carbon atom, while the O atom was adsorbed to the carbon atom closest to the Cu atom. The most stable CH + O co-adsorption geometry on the CuG surface was presented in Fig. 3j. The stable equilibrium distance between CH–O was 3.17 Å. On the other hand, the co-

adsorption energy of CH + O on the CuG surface was obtained as −7.24 eV.

Possible reaction mechanism for CH_3OH decomposition on CuG

A number of consecutive steps can occur during the decomposition of the CuG surface adsorbed CH3OH to obtain various intermediate species. The decomposition reaction involves cleavage the C–H, C–O and O–H bonds of CH_3OH. The reaction pathway initially starts with the cleavage of the C–O bond to obtain CH_3 and OH intermediates and continues through the activation of the O–H bond. It should be noted that the activation of the C–H bond was not investigated in this study because of the formation of CH2OH and H intermediates at the end of the reaction.

Following the determining the adsorption and co-adsorption sites on the surface for the intermediate states, the transition state energies (E_a) and reaction energies (E_r) of the intermediate states constituting the reaction mechanism were calculated. Since the CINEB method allows the calculation of the activation and reaction energy needed for all possible steps on the reaction pathway, all calculations in this study were investigated by the CINEB method. For all possible steps, initial state (IS), final state (FS) and transition state (TS) structures were depicted in Fig. 4, and the obtained results were given in Table 4. For intermediate states on the reaction pathway, IS and FS structures were considered as their geometry corresponding to their most stable regions on the surface.

The cleavage of C–O and O–H bonds of CH_3OH

The decomposition reaction begun with the cleavage of the C–O bond of CH_3OH. Afterward, two possible cases for cleavage of the O–H bond were examined. O–H bond cleavage was investigated both on the CuG surface and in the presence of previously adsorbed oxygen on the surface.

For the cleavage of the C–O bond of CH_3OH, the most stable adsorption geometry of CH_3OH adsorbed on the CuG surface was proposed as the initial state of the reaction (Fig. 2a). The CH_3OH molecule was decomposed into CH_3 and OH as a result of the cleavage of the C–O bond (Fig. 3c). The results showed that the activation energy needed for the $CH_3OH \rightarrow TS1 \rightarrow CH_3+OH$ reaction to occur is 0.82 eV. This reaction step was carried out endothermically with a reaction energy of 0.45 eV. In the presence of oxygen, the co-adsorption geometry (Fig. 3b), in which CH_3OH and O are adsorbed to the CuG surface, was considered as the initial state (IS). Moreover, the CH_3O + OH co-adsorption geometry (Fig. 3a) obtained by cleavage of the O–H bond was determined as the end state (FS).

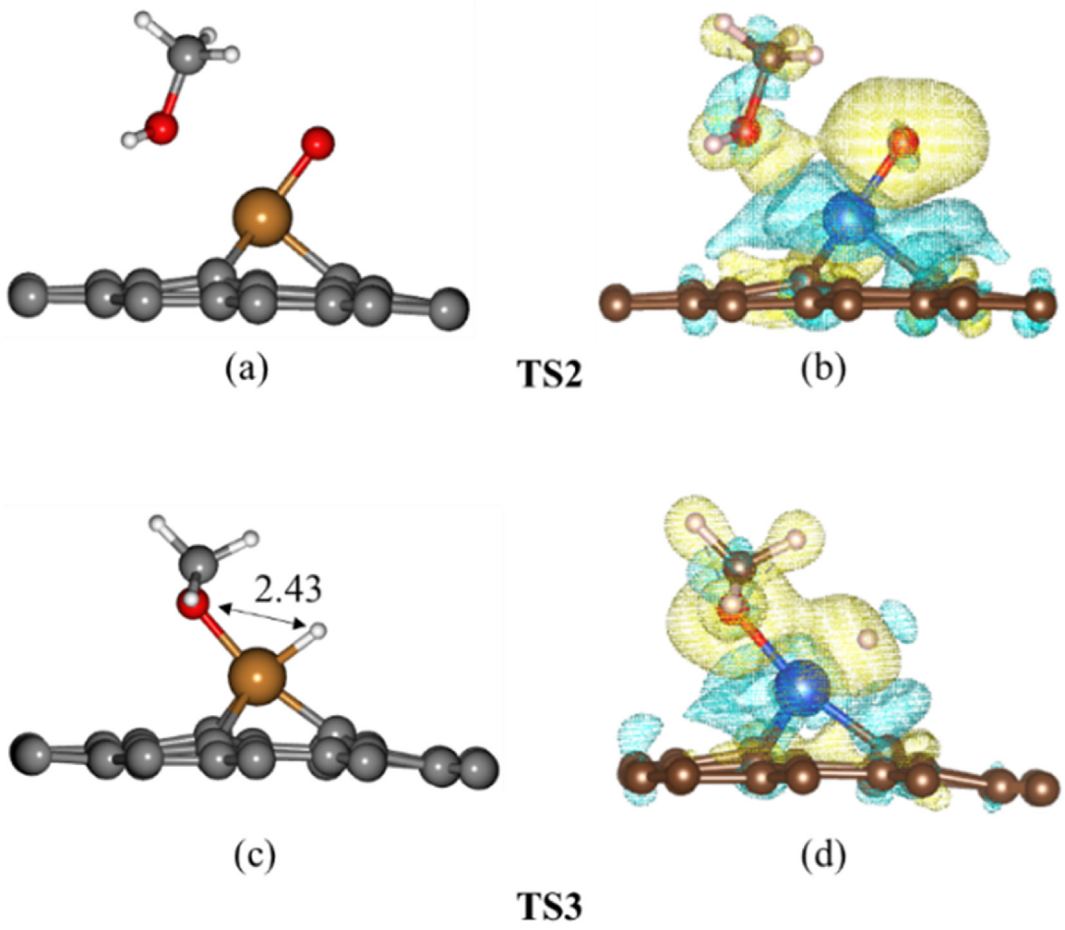

Fig. 4 – Transition state geometries of (a) CH_3OH + O →TS2 → CH_3O + OH, (c) CH_3OH →TS3 → CH_3O + H, and EDD maps both for (b) CH_3OH + O →TS2 → CH_3O + OH, (d) CH_3OH →TS3 → CH_3O + H reaction pathways on CuG surface(±0.016 au).

Table 4 – Activation and reaction energies of CH_3OH decomposition reactions on CuG.

Reaction pathway for CH_3OH decomposition		Activation energy Ea/eV	Reaction energy Er/eV
CH_3OH	$CH_3OH \rightarrow TS1 \rightarrow CH_3+OH$	0.82	0.45
$CH_3OH + O \rightarrow CH_3O + OH$	$CH_3OH + O \rightarrow TS2 \rightarrow CH_3O + OH$	0.008	−1.06
$CH_3OH \rightarrow CH_3O + H$	$CH_3OH \rightarrow TS3 \rightarrow CH_3O + H$	1.19	1.09
$CH_3O \rightarrow CH_3+O$	$CH_3O \rightarrow TS4 \rightarrow CH_3+O$	1.98	1.53
$CH_3O \rightarrow CH_2O + H$	$CH_3O \rightarrow TS5 \rightarrow CH_2O + H$	1.47	1.45
$CH_2O \rightarrow CHO + H$	$CH_2O \rightarrow TS6 \rightarrow CHO + H$	0.78	0.71
$CH_2O \rightarrow CH_2+O$	$CH_2O \rightarrow TS7 \rightarrow CH_2+O$	1.73	1.66
$CHO \rightarrow CH + O$	$CHO \rightarrow TS8 \rightarrow CH + O$	2.17	1.53
$CHO \rightarrow CO + H$	$CHO \rightarrow TS9 \rightarrow CO + H$	0.25	0.13

The transition state geometry (TS2) was represented in Fig. 4a. According to TS2's Bader charge analysis, the electron transfer from surface to the reactant at the transition state was determined as to be 0.72 |e|. Fig. 4b represented the redistribution of the electron density of the surface after electron transfer. As a result, it could be realized that some of the electrons transported from the surface accumulated on the O–H bond. This charge transfer led the O–H bond to be elongated from 0.97 Å to 0.975 Å relative to its initial state. The findings revealed that the activation and reaction energies of the reaction on the CuG surface were 0.008 eV and −1.06 eV, respectively. The negative value of the reaction energy indicated that this reaction step took place exothermically.

In the second reaction step, the catalytic activity of the CuG surface towards the O–H bond was investigated. The most stable adsorption geometry of CH_3OH on the CuG surface was considered to be the initial state of the reaction (Fig. 2a). The co-adsorption geometry of CH_3O and H, which was obtained by breaking the O–H bond, was determined as the final state of the reaction (Fig. 3d). In the transition state (TS3), an electron transfer of 0.54 |e| took place from the surface to the reactant. The distance between O–H at the transition state was calculated to be 2.43 Å (Fig. 4c). The activation energy required to break the O–H bond on the CuG surface was found to be 1.19 eV. In addition, this reaction step was occurred endothermically with a reaction energy of 1.09 eV.

As can be seen in Fig. 4b and d, the electron density redistribution of TS2 was much larger than that of TS3. This finding revealed that, in accordance with the values given in Table 4, the interaction of the reactant in TS2 with the CuG surface was much stronger than the reactant in TS3.

All these calculations proved that the CuG surface offered satisfactory catalytic activity towards C–O and O–H bonds. As a result, the methanol decomposition reaction mechanism on the proposed CuG catalyst proceeded via $CH_3OH \rightarrow CH_3O \rightarrow CH_2O \rightarrow CHO \rightarrow CO$ by cleavage of the O–H bond.

Decomposition of CH_3O

Two possible cases for CH_3O decomposition were examined.

Case I: $CH_3O \rightarrow CH_3 + O$; In this reaction step, the CH_3O molecule adsorbed on the CuG surface was accepted as the initial state of the reaction. C–O bond cleavage led to the formation of the CH_3+O intermediate state and they were considered as the final state of this reaction step. The transition state geometry and the electron density difference map were shown in Fig. 5.

In the transition state (TS4), the distance between the O atom and the carbon was found to be 1.84 Å (Fig. 5a). An electron transfer of 0.48 |e| took place from the surface to the reactants. According to Fig. 5b, this charge transfer caused the O to have strong chemical interactions with both the carbon and Cu atom, and the C–O bond was broken with a high activation energy of 1.98 eV. In addition, this reaction was determined to be endothermic with a reaction energy of 1.53 eV.

Case II: $CH_3O \rightarrow CH_2O + H$, By the cleavage of the C–H bond, the CH_3O molecule was decomposed into CH_2O + H species which were considered as the initial and final state geometries of this reaction step, respectively. At the transition state (TS5), the distance between the split hydrogen atom and O was found to be 2.51 Å (Fig. 5c). According to the Bader charge analysis, an electron transfer of 0.72 |e| from the surface to the reactants occurred. In Fig. 5d, it was seen that a significant electron density was accumulated on the decomposed hydrogen atom. Compared to the C–O bond, this charge transfer led the C–H bond to be broken down with a lower activation energy of 1.47 eV. Moreover, it was determined that this reaction took place endothermically with a reaction energy of 1.45 eV.

Decomposition of CH_2O

Two possible reaction pathways were considered, which were the cleavage of the C–O or C–H bonds of the CH2O molecule adsorbed on the CuG surface.

Case I: $CH_2O \rightarrow CH_2 + O$; The most stable adsorption geometry of the CH_2O molecule adsorbed on the CuG surface was considered as the initial state of the reaction (Fig. 2c). As a result of C–O bond cleavage, the CH_2O molecule was broken down into CH_2 and O species. The geometry of this co-adsorption with minimum energy (Fig. 3g) was determined as the final state of the reaction. In the transition state (TS6), the decomposed oxygen atom was found to be 3 Å away from the carbon atom (Fig. 6a). The results showed that the activation barrier needed for the $CH_2O \rightarrow CH_2$+O reaction to occur was to be 1.73 eV. In addition, this reaction took place endothermically with a reaction energy of 1.66 eV.

Case II: $CH_2O \rightarrow CHO$ H; In this reaction step, the most stable adsorption geometries of CH_2O and CHO + H species were considered as the initial and final states of the reaction, respectively.

In the transition state (TS7), as a result of the cleavage of the C–H bond, the CHO molecule was attached to the surface

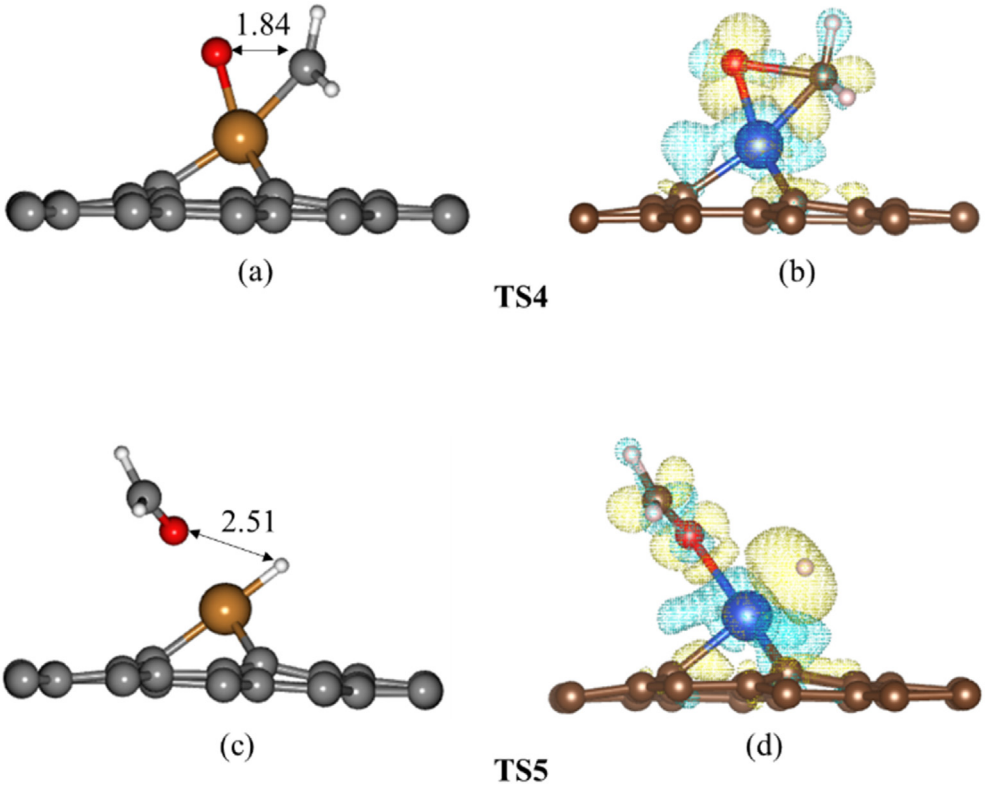

Fig. 5 – Transition state geometries of (a)$CH_3O \rightarrow TS4 \rightarrow CH_3 + O$, (c) $CH_3O \rightarrow TS5 \rightarrow CH_2O + H$, and EDD maps both for (b) $CH_3O \rightarrow TS4 \rightarrow CH_3 + O$, (d) $CH_3O \rightarrow TS5 \rightarrow CH_2O + H$ reaction pathways on CuG surface (±0.016 au).

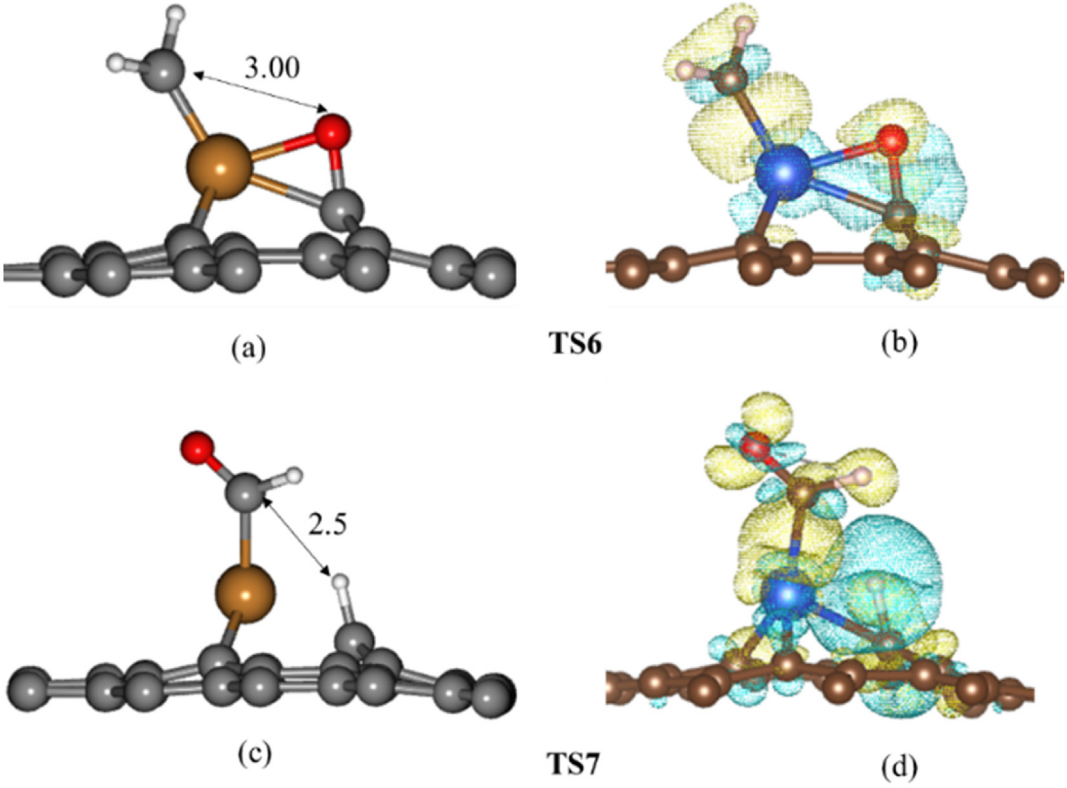

Fig. 6 – Transition state geometries of (a) $CH_2O \rightarrow TS6 \rightarrow CH_2 + O$, (c) $CH_2O \rightarrow TS7 \rightarrow CHO + H$, and EDD maps both for (b) $CH_2O \rightarrow TS6 \rightarrow CH_2 + O$, (d) $CH_2O \rightarrow TS7 \rightarrow CHO + H$ reaction pathways on CuG surface (±0.002 au).

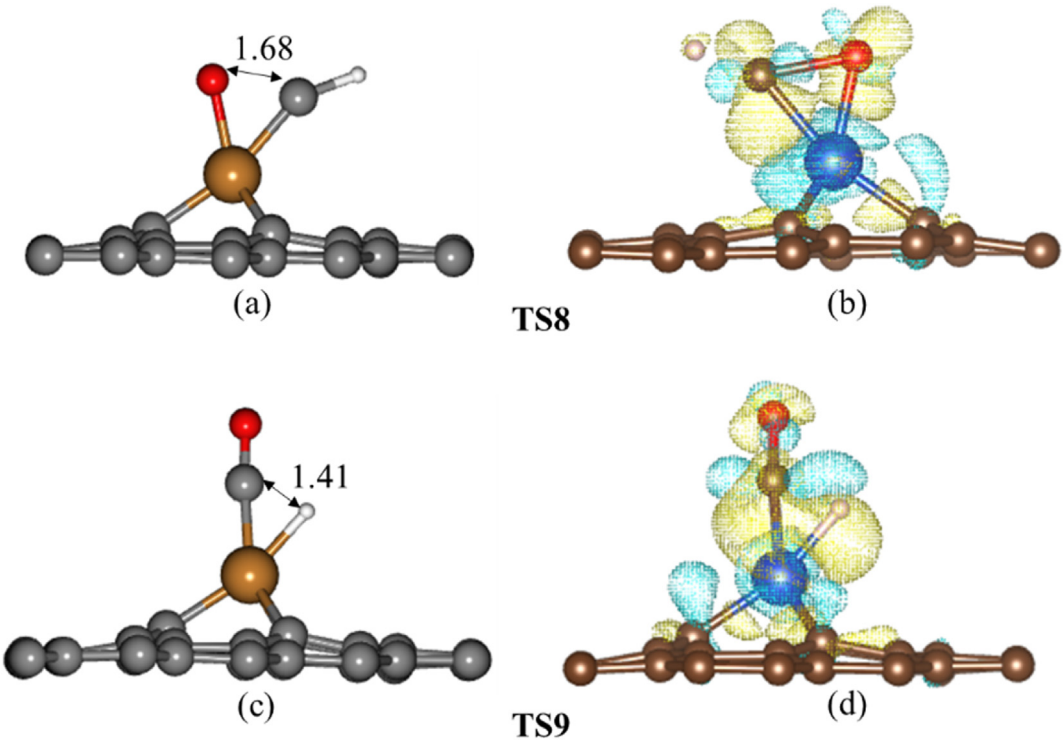

Fig. 7 – Transition state geometries of (a) CHO →TS8 → CH + O, (c) CHO →TS9 → CO + H, and EDD maps both for (b) CHO →TS8 → CH + O, (d) CHO →TS9 → CO + H reaction pathways on CuG surface(±0.002 au).

by the Cu atom, whereas the H atom preferred to be attached to one of the carbon atoms closest to the Cu atom (Fig. 6c). The activation energy required for CH_2O → CHO + H reaction was calculated to be 0.78 eV. Moreover, it was determined that this reaction step was endothermic with a reaction energy of 0.66 eV. When the EDD maps of both reaction steps shown in Fig. 6b and d were compared, it was determined that the electron distribution redistribution pattern of TS7 was larger than that of TS6. This result revealed that the reactants in TS7 interacted more strongly with the surface than the reactants in TS6. The obtained results were in good agreement with the values listed in Table 4.

Decomposition of CHO

CHO decomposition on the CuG surface was considered in two possible steps via cleavage of C–H and C–O bonds. Both of the transition state geometries were shown in Fig. 7a and Fig. 7c.

As a result of the cleavage of the C–O bond, the CHO molecule was decomposed into CH + O species. In the transition state (TS8), it was found that the split O atom was 1.68 Å away from the carbon atom. According to the results of Bader analysis of the transition state on the CuG surface, an electron transfer of 0.31 |e| from the surface to the molecule was observed. The electron redistribution of the surface after charge transfer was shown in Fig. 7b.

It was realized that the electrons transferred from the surface were acummulated on the Cu–CH and Cu–O bonds. Accordingly, it could be concluded that oxygen was in a strong bonding state with both carbon and Cu atoms in the transition state. The activation energy needed for the CHO → CH + O reaction to take place was calculated as 2.17 eV. In addition, it was observed that this reaction occurred endothermically with a reaction energy of 1.53 eV.

As a result of the cleavage of the C–H bond, the CHO molecule could be broken down into CO + H species, and these were considered to be the initial and the final state of the reaction step, respectively. In the transition state (TS9), the hydrogen atom detached from the CHO molecule preferred to adsorb to the Cu atom on the CuG surface. The distance between CO–H in the transition state was determined as to be 1.41 Å. According to the Bader charge analysis, an electron transfer of 0.52 |e| occurred from the surface to the molecule. According to this charge transfer, it was seen that a significant part of the electrons transferred from the surface was intense on the C–H bond, as shown in Fig. 7d. Moreover, it should be emphasized that this charge transfer might have weakened the C–H bond, thereby causing the hydrogen to break down from the structure more easily. The energy barrier required for the CHO →CO + H reaction to occur was calculated to be 0.25 eV. In addition, this reaction step was determined to occur endothermically with a reaction energy of 0.13 eV.

Brief summary

Decomposition of CH3OH entails breaking the C–H, O–H, and C–O bonds in its structure. The findings revealed that the C–O bond cleavage (with an activation energy of 0.82 eV) occurred more easily compared to other bonds. In the initial state, the O–H bond of the CH_3OH molecule on the CuG surface decomposed with an energy of 1.19 eV. Moreover, it was determined that the activation barrier values of C–O and O–H were close to each other. Therefore, the CH_3OH

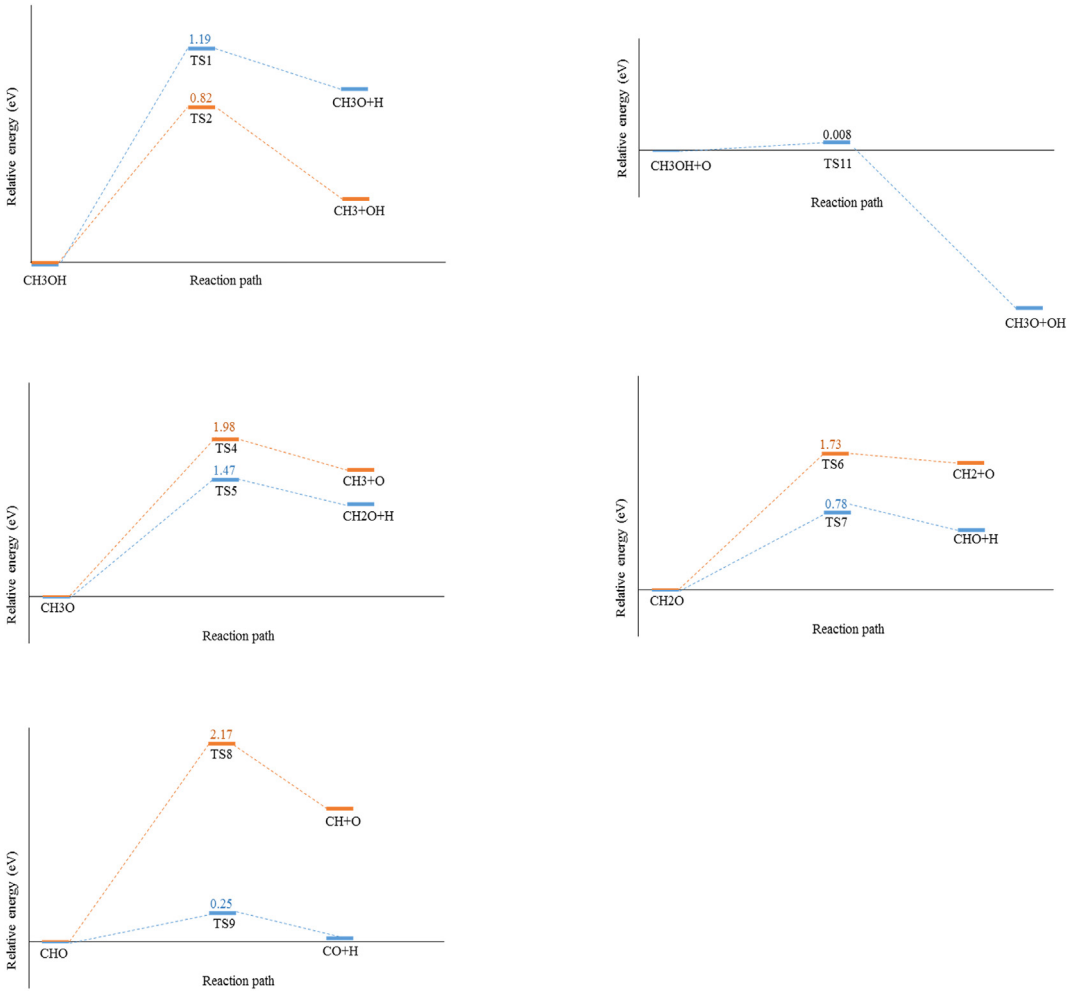

Fig. 8 – Relative energy profiles for CH_3OH decomposition on CuG graphene surfaces.

decomposition reaction mechanism on the proposed CuG catalyst surface was established on the basis of the cleavage of the O–H bond. The as-calculated activation energies for all possible states on the reaction pathway were presented in Fig. 8. Accordingly, although C–O bond cleavage was seemed to be the favorite, when different conditions were examined, for example, in the case of O–H bond cleavage, in the presence of oxygen previously adsorbed to the surface, it was observed that the O–H bond was broken with a very small energy barrier of 0.008 eV.

When the decomposition of CH3O was examined, it was found that the C–O and C–H bonds were cleaved with activation energies of 1.98 eV and 1.47 eV, respectively (Fig. 8). For the transition states of $CH_3O \rightarrow CH_3{+}O$ and $CH_3O \rightarrow CH_2O + H$, the electron transfers of 0.45 |e| and 0.72 |e| from the surface to the reactants occurred, respectively. After this charge transfer, the C–H bond became more activated, and the C–H bond on the CuG surface was more easily cleaved compared to the C–O bond.

On the other hand, when CH_2O decomposition was investigated, it was determined that the C–O and C–H bonds were broken with the activation barriers of 1.73 eV and 0.78 eV, respectively. Moreover, the EDD maps presented in Fig. 6b and d showed that the TS7 configuration interacted more strongly with the surface than TS6. As a result, these interactions led further weakening of the C–H bond, thereby the C–H bond was more easily cleaved than the C–O bond.

For CHO decomposition, C–O and C–H bond cleavages have an energy barrier of 2.17 eV and 0.25 eV, respectively. It could be said that this significant difference in activation energies caused the strong interactions between C–Cu and Cu–O after an electron transfer of 0.31 |e| from the surface as shown in Fig. 7b. Therefore, the C–O bond was cleaved with relatively higher activation energy. During the C–H bond cleavage of the CHO molecule, electron transfer of 0.52 |e| occurred from the surface. On the EDD map shown in Fig. 7d, it was seen that a significant part of this charge was intense on the C–H bond. It could be clearly stated that this charge transfer weakened the C–H bond considerably.

Conclusion

In this study, the decomposition of CH_3OH on the CuG catalyst surface was investigated in detail through density functional theory. The electron density difference map of the CuG surface revealed that a positive charge density of 0.65 |e| occurred around the Cu atom. Therefore, intermediate state molecules

including CH_3OH and CH_3O, CH_2O and CHO tended to be adsorbed around the Cu sites of the catalyst surface. In the initial state, the C–O and C–H bonds of CH_3OH offered the lowest activation barriers. However, it was determined that the adsorbing of oxygen to the surface caused the CuG surface to show very high catalytic activity on the O–H bonds of CH_3OH. Therefore, it was concluded that the CH_3OH decomposition reaction on the proposed CuG catalyst proceeded through $CH_3OH \rightarrow CH_3O \rightarrow CH_2O \rightarrow CHO \rightarrow CO$ path as the most likely case. In brief, the results obtained for the decomposition of CH_3OH on the CuG surface demonstrated that the CuG surface may be an ideal catalyst candidate and can be utilized as an alternative catalyst to reduce the CO poisoning problem of direct methanol fuel cells.

Declaration of competing interest

The authors declare that they have no known competing financial interests or personal relationships that could have appeared to influence the work reported in this paper.

Acknowledgment

The numerical calculations reported in this paper were fully performed at TUBITAK ULAKBIM, High Performance and Grid Computing Center (TRUBA resources).

REFERENCES

[1] Al-Zareer M, Dincer I, Rosen MA. Transient thermodynamic analysis of a novel integrated ammonia production, storage and hydrogen production system. Int J Hydrogen Energy 2019;44:18214–24.
[2] Acar C, Dincer I. Review and evaluation of hydrogen production options for better environment. J Clean Prod 2019;218:835–49.
[3] Dincer I, Acar C. Review and evaluation of hydrogen production methods for better sustainability. Int J Hydrogen Energy 2015;40:11094–111.
[4] Gopalsamy K, Subramanian V. Hydrogen storage capacity of alkali and alkaline earth metal ions doped carbon based materials: a DFT study. Int J Hydrogen Energy 2014;39:2549–59.
[5] Bicer Y, Dincer I. Comparative life cycle assessment of hydrogen, methanol and electric vehicles from well to wheel (vol 42, pg 3767, 2017). Int J Hydrogen Energy 2017;42:14841.
[6] Dincer I, Rosen MA. Sustainability aspects of hydrogen and fuel cell systems. Energy Sustain Dev 2011;15:137–46.
[7] Granovskii M, Dincer I, Rosen MA. Life cycle assessment of hydrogen fuel cell and gasoline vehicles. Int J Hydrogen Energy 2006;31:337–52.
[8] Damte JY, Lyu SL, Leggesse EG, Jiang JC. Methanol decomposition reactions over a boron-doped graphene supported Ru-Pt catalyst. Phys Chem Chem Phys 2018;20:9355–63.
[9] Moura AS, Fajin JLC, Pinto ASS, Mandado M, Cordeiro MNDS. Competitive paths for methanol decomposition on ruthenium: a DFT study. J Phys Chem C 2015;119:27382–91.
[10] Pang K, Ren RP, Lv YK. DFT study on the mechanism of methanol decomposition catalyzed by Mo-CNTs. Mater Today Commun 2020;25.
[11] Olah GA. Beyond oil and gas: the methanol economy. Angew Chem Int Ed 2005;44:2636–9.
[12] Edwards PP, Kuznetsov VL, David WIF, Brandon NP. Hydrogen and fuel cells: towards a sustainable energy future. Energy Pol 2008;36:4356–62.
[13] Gallucci F, Basile A, Drioli E. Methanol as an energy source and/or energy carrier in membrane processes. Separ Purif Rev 2007;36:175–202.
[14] Holton OT, Stevenson JW. The Role of Platinum in Proton Exchange Membrane Fuel Cells Evaluation of platinum's unique properties for use in both the anode and cathode of a proton exchange membrane fuel cell. Platin Met Rev 2013;57:259–71.
[15] Garcia-Rates M, Garcia-Muelas R, Lopez N. Solvation effects on methanol decomposition on Pd(111), Pt(111), and Ru(0001). J Phys Chem C 2017;121:13803–9.
[16] Sexton BA. Methanol decomposition on platinum (111). Surf Sci 1981;102:271–81.
[17] Lu GQ, Chrzanowski W, Wieckowski A. Catalytic methanol decomposition pathways on a platinum electrode. J Phys Chem B 2000;104:5566–72.
[18] Miller AV, Kaichev VV, Prosvirin IP, Bukhtiyarov VI. Mechanistic study of methanol decomposition and oxidation on Pt(111). J Phys Chem C 2013;117:8189–97.
[19] Avgouropoulos G, Papavasiliou J, Ioannides T. Hydrogen production from methanol over combustion-synthesized noble metal/ceria catalysts. Chem Eng J 2009;154:274–80.
[20] Feng H, Elam JW, Libera JA, Setthapun W, Stair PC. Palladium catalysts synthesized by atomic layer deposition for methanol decomposition. Chem Mater 2010;22:3133–42.
[21] Liu D, Men Y, Wang JG, Kolb G, Liu X, Wang YQ, et al. Highly active and durable Pt/In2O3/Al2O3 catalysts in methanol steam reforming. Int J Hydrogen Energy 2016;41:21990–9.
[22] Patel N, Patton B, Zanchetta C, Fernandes R, Guella G, Kale A, et al. Pd-C powder and thin film catalysts for hydrogen production by hydrolysis of sodium borohydride. Int J Hydrogen Energy 2008;33:287–92.
[23] Antolini E, Lopes T, Gonzalez ER. An overview of platinum-based catalysts as methanol-resistant oxygen reduction materials for direct methanol fuel cells. J Alloys Compd 2008;461:253–62.
[24] Li YJ, Gao W, Ci LJ, Wang CM, Ajayan PM. Catalytic performance of Pt nanoparticles on reduced graphene oxide for methanol electro-oxidation. Carbon 2010;48:1124–30.
[25] Xin YC, Liu JG, Zhou Y, Liu WM, Gao JA, Xie Y, et al. Preparation and characterization of Pt supported on graphene with enhanced electrocatalytic activity in fuel cell. J Power Sources 2011;196:1012–8.
[26] Liu ZX, Sawada T, Takagi N, Watanabe K, Matsumoto Y. Reaction intermediates in the oxidation of methanol on a Pt(111)-(2x2)O surface. J Chem Phys 2003;119:4879–86.
[27] Akhter S, White JM. A static sims Tpd study of the kinetics of methoxy formation and decomposition on O/Pt(111). Surf Sci 1986;167:101–26.
[28] Wang JH, Masel RI. Methanol adsorption and decomposition on (2 X-1) Pt(110) - enhanced stability of the methoxy intermediate on a stepped surface. Surf Sci 1991;243:199–209.
[29] Diekhoner L, Butler DA, Baurichter A, Luntz AC. Parallel pathways in methanol decomposition on Pt(111). Surf Sci 1998;409:384–91.
[30] Skoplyak O, Menning CA, Barteau MA, Chen JGG. Experimental and theoretical study of reactivity trends for methanol on Co/Pt(111) and Ni/Pt(111) bimetallic surfaces. J Chem Phys 2007;127.

[31] Kua J, Goddard WA. Oxidation of methanol on 2nd and 3rd row Group VIII transition metals (Pt, Ir, Os, Pd, Rh, and Ru): application to direct methanol fuel cells. J Am Chem Soc 1999;121:10928–41.
[32] Greeley J, Mavrikakis M. Competitive paths for methanol decomposition on Pt(111). J Am Chem Soc 2004;126:3910–9.
[33] Ishikawa Y, Liao MS, Cabrera CR. Oxidation of methanol on platinum, ruthenium and mixed Pt-M metals (M = Ru, Sn): a theoretical study. Surf Sci 2000;463:66–80.
[34] Delbecq F, Sautet P. A density functional study of adsorption structures of unsaturated aldehydes on Pt(111): a key factor for hydrogenation selectivity. J Catal 2002;211:398–406.
[35] Antolini E. Graphene as a new carbon support for low-temperature fuel cell catalysts. Appl Catal B Environ 2012;123:52–68.
[36] Dong LF, Gari RRS, Li Z, Craig MM, Hou SF. Graphene-supported platinum and platinum-ruthenium nanoparticles with high electrocatalytic activity for methanol and ethanol oxidation. Carbon 2010;48:781–7.
[37] Yang SL, Liu YA, Lei G, Xie YL, Peng LP, Xu HX, et al. A DFT study on the hydrogen storage performance of MoS2 monolayers doped with group 8B transition metals. Int J Hydrogen Energy 2021;46:24233–46.
[38] Kaplan BY, Haghmoradi N, Bicer E, Merino C, Gursel SA. High performance electrocatalysts supported on graphene based hybrids for polymer electrolyte membrane fuel cells. Int J Hydrogen Energy 2018;43:23221–30.
[39] Gong XB, Peng L, Wang XH, Wu LL, Liu Y. Duckweed derived nitrogen self-doped porous carbon materials as cost-effective electrocatalysts for oxygen reduction reaction in microbial fuel cells. Int J Hydrogen Energy 2020;45:15336–45.
[40] Orooji Y, Gol HG, Jaleh B, Vaziri MRR, Eslamipanah M. Large optical nonlinearity of the activated carbon nanoparticles prepared by laser ablation. Nanomaterials 2021:11.
[41] Sohrabi H, Khataee A, Ghasemzadeh S, Majidi MR, Orooji Y. Layer double hydroxides (LDHs)- based electrochemical and optical sensing assessments for quantification and identification of heavy metals in water and environment samples: a review of status and prospects. Trends Environ Anal Chem 2021;31:e00139.
[42] Taherian Z, Khataee A, Orooji Y. Nickel-based nanocatalysts promoted over MgO-modified SBA-16 for dry reforming of methane for syngas production: impact of support and promoters. J Energy Inst 2021;97:100–8.
[43] Taherian Z, Gharahshiran VS, Khataee A, Orooji Y. Anti-coking freeze-dried NiMgAl catalysts for dry and steam reforming of methane. J Ind Eng Chem 2021;103:187–94. https://doi.org/10.1016/j.jiec.2021.07.032.
[44] Gupta VK, Eren T, Atar N, Yola ML, Parlak C, Karimi-Maleh H. CoFe2O4@TiO2 decorated reduced graphene oxide nanocomposite for photocatalytic degradation of chlorpyrifos. J Mol Liq 2015;208:122–9.
[45] Yola ML, Atar N, Eren T, Karimi-Maleh H, Wang SB. Sensitive and selective determination of aqueous triclosan based on gold nanoparticles on polyoxometalate/reduced graphene oxide nanohybrid (vol 5, pg 65953, 2015). RSC Adv 2015;5:72590–1.
[46] Karimi-Maleh H, Shafieizadeh M, Taher MA, Opoku F, Kiarii EM, Govender PP, et al. The role of magnetite/graphene oxide nano-composite as a high-efficiency adsorbent for removal of phenazopyridine residues from water samples, an experimental/theoretical investigation. J Mol Liq 2020:298.
[47] Khodadadi A, Faghih-Mirzaei E, Karimi-Maleh H, Abbaspourrad A, Agarwal S, Gupta VK. A new epirubicin biosensor based on amplifying DNA interactions with polypyrrole and nitrogen-doped reduced graphene: experimental and docking theoretical investigations. Sensor Actuator B Chem 2019;284:568–74.
[48] Zhao YG, Li L, Liu DK, Wu ZH, Wang YX, Liu JJ, et al. Sponge tofu-like graphene-carbon hybrid supporting Pt-Co nanocrystals for efficient oxygen reduction reaction and Zn-Air battery. Int J Hydrogen Energy 2021;46:15561–71.
[49] Shi CJ, Maimaitiyiming X. Three dimensional nitrogen, phosphorus and sulfur doped porous graphene as efficient bifunctional electrocatalysts for direct methanol fuel cell. Int J Hydrogen Energy 2021;46.
[50] Karaman C. Orange peel derived-nitrogen and sulfur Co-doped carbon dots: a nano-booster for enhancing ORR electrocatalytic performance of 3D graphene networks. Electroanalysis 2021;33(5):1356–69. https://doi.org/10.1002/elan.202100018.
[51] Karaman O. Oxygen reduction reaction performance boosting effect of nitrogen/sulfur Co-doped graphene supported cobalt phosphide nanoelectrocatalyst: pH-universal electrocatalyst. **ECS J** Solid State Sci Technol 2021;10.
[52] Akca A, Karaman O, Karaman C. Mechanistic insights into catalytic reduction of N2O by CO over Cu-embedded graphene: a density functional theory perspective. ECS J Solid State Sci Technol 2021;10(4):041003.
[53] Esrafili MD, Asadollahi S, Heydari S. A DFT study on NO reduction to N2O using Al- and P-doped hexagonal boron nitride nanosheets. J Mol Graph Model 2019;89:41–9.
[54] Liu Z, Cheng XR, Yang YM, Jia HZ, Bai BQ, Zhao L. DFT study of N2O adsorption onto the surface of M-decorated graphene oxide (M = Mg, Cu or Ag). Materials 2019;12.
[55] Nemiwal M, Zhang TC, Kumar D. Graphene-based electrocatalysts: hydrogen evolution reactions and overall water splitting. Int J Hydrogen Energy 2021;46:21401–18.
[56] Palani R, Karuppiah C, Yang CC, Piraman S. Metal-organic frameworks derived spinel NiCo2O4/graphene nanosheets composite as a bi-functional cathode for high energy density LieO(2) battery applications. Int J Hydrogen Energy 2021;46:14288–300.
[57] Karaman C, Karaman O, Atar N, Yola ML. Tailoring of cobalt phosphide anchored nitrogen and sulfur Co-doped three dimensional graphene hybrid: boosted electrocatalytic performance towards hydrogen evolution reaction. Electrochim Acta 2021;380:138262.
[58] Zhong JP, Wu LY, Lan JJ, Waqas M, Sun ML, Fan YJ, et al. Worm-like Pt nanoparticles anchored on graphene with S, N co-doping and Fe3O4 functionalization for boosting the electrooxidation of methanol. Int J Hydrogen Energy 2020;45:22929–37.
[59] Jia TT, Lu CH, Zhang YF, Chen WK. A comparative study of CO catalytic oxidation on Pd-anchored graphene oxide and Pd-embedded vacancy graphene. J Nanoparticle Res 2014;16:1–11.
[60] Jiang QG, Zhang JF, Ao ZM, Huang HJ, He HY, Wu YP. First principles study on the CO oxidation on Mn-embedded divacancy graphene. Front Chem 2018;6:187.
[61] Miao M, Gong XJ, Lei SL, Wang L, Sha ML, Meng QQ. The graphene-supported non-noble metal catalysts activate ammonia decomposition: a DFT study. Chem Phys 2021:548.
[62] Kocer T, Oztuna FES, Kurtoglu SF, Unal U, Uzun A. Graphene aerogel-supported ruthenium nanoparticles for COx-free hydrogen production from ammonia. Appl Catal Gen 2021:610.

[63] Yao QL, Ding YY, Lu ZH. Noble-metal-free nanocatalysts for hydrogen generation from boron- and nitrogen-based hydrides. Inorg Chem Front 2020;7:3837–74.
[64] Lu YH, Zhou M, Zhang C, Feng YP. Metal-embedded graphene: a possible catalyst with high activity. J Phys Chem 2009;113:20156–60.
[65] Zhou M, Lu YH, Cai YQ, Zhang C, Feng YP. Adsorption of gas molecules on transition metal embedded graphene: a search for high-performance graphene-based catalysts and gas sensors. Nanotechnology 2011;22.
[66] Liu X, Sui YH, Duan T, Meng CG, Han Y. CO oxidation catalyzed by Pt-embedded graphene: a first-principles investigation. Phys Chem Chem Phys 2014;16:23584–93.
[67] Ghasali E, Ghahremani D, Orooji Y. Using metallic additives as a bonding layer to produce Ti-based laminated composites via spark plasma sintering. J Sci: Adv Mater Devices 2021;6:435–45.
[68] Wannakao S, Nongnual T, Khongpracha P, Maihom T, Limtrakul J. Reaction mechanisms for CO catalytic oxidation by N2O on Fe-embedded graphene. J Phys Chem C 2012;116:16992–8.
[69] Sirijaraensre J, Limtrakul J. Hydrogenation of CO2 to formic acid over a Cu-embedded graphene: a DFT study. Appl Surf Sci 2016;364:241–8.
[70] Cao HJ, Bai H, Bai B, Ma MM, Bai B, Ling LX, et al. Syngas conversion catalyzed by copper-embedded graphene. Appl Surf Sci 2020:525.
[71] Li JY, Tang XL, Yi HH, Yu QJ, Gao FY, Zhang RC, et al. Effects of copper-precursors on the catalytic activity of Cu/graphene catalysts for the selective catalytic oxidation of ammonia. Appl Surf Sci 2017;412:37–44.
[72] Song EH, Wen Z, Jiang Q. CO catalytic oxidation on copper-embedded graphene. J Phys Chem C 2011;115:3678–83.
[73] Wang L, Luo QQ, Zhang WH, Yang JL. Transition metal atom embedded graphene for capturing CO: a first-principles study. Int J Hydrogen Energy 2014;39:20190–6.
[74] Zuo ZJ, Wang L, Han PD, Huang W. Insights into the reaction mechanisms of methanol decomposition, methanol oxidation and steam reforming of methanol on Cu(111): a density functional theory study. Int J Hydrogen Energy 2014;39:1664–79.
[75] Ren RP, Zhang YC, Liu SZ, Zuo ZJ, Lv YK. DFT studies of the methanol decomposition mechanism on the H2O/Cu(110) and OH pre-adsorbed H2O/Cu(110) interfaces: comparison with the clean Cu(110) surface. Int J Hydrogen Energy 2016;41:2411–23.
[76] Giannozzi P, Andreussi O, Brumme T, Bunau O, Nardelli MB, Calandra M, et al. Advanced capabilities for materials modelling with QUANTUM ESPRESSO. J Phys Condens Matter 2017;29:465901.
[77] Giannozzi P, Baroni S, Bonini N, Calandra M, Car R, Cavazzoni C, et al. Quantum ESPRESSO: a modular and open-source software project for quantum simulations of materials. J Phys Condens Matter 2009;21:395502.
[78] Kresse G, Joubert D. From ultrasoft pseudopotentials to the projector augmented-wave method. Phys Rev B 1999;59:1758–75.
[79] Monkhorst HJ, Pack JD. Special points for brillouin-zone integrations. Phys Rev B 1976;13:5188–92.
[80] Grimme S, Antony J, Ehrlich S, Krieg H. A consistent and accurate ab initio parametrization of density functional dispersion correction (DFT-D) for the 94 elements H-Pu. J Chem Phys 2010;132:154104.
[81] Henkelman G, Arnaldsson A, Jonsson H. A fast and robust algorithm for Bader decomposition of charge density. Comput Mater Sci 2006;36:354–60.
[82] Henkelman G, Uberuaga BP, Jonsson H. A climbing image nudged elastic band method for finding saddle points and minimum energy paths. J Chem Phys 2000;113:9901–4.
[83] Yang CK. A metallic graphene layer adsorbed with lithium. Appl Phys Lett 2009;94.
[84] Santos EJ, Ayuela A, Sánchez-Portal D. First-principles study of substitutional metal impurities in graphene: structural, electronic and magnetic properties. New J Phys 2010;12:053012.